



1 **Interpretation of geostationary satellite aerosol optical depth**  
2 **(AOD) over East Asia in relation to fine particulate matter**  
3 **(PM<sub>2.5</sub>): insights from the KORUS-AQ aircraft campaign and**  
4 **seasonality**

5 Shixian Zhai<sup>1</sup>, Daniel J. Jacob<sup>1</sup>, Jared F. Brewer<sup>1</sup>, Ke Li<sup>1</sup>, Jonathan M. Moch<sup>1</sup>, Jhoon Kim<sup>2, 3</sup>,  
6 Seoyoung Lee<sup>2</sup>, Hyunkwang Lim<sup>2</sup>, Hyun Chul Lee<sup>3</sup>, Su Keun Kuk<sup>3</sup>, Rokjin J. Park<sup>4</sup>, Jaemin I.  
7 Jeong<sup>4</sup>, Xuan Wang<sup>5</sup>, Pengfei Liu<sup>6</sup>, Gan Luo<sup>7</sup>, Fangqun Yu<sup>7</sup>, Jun Meng<sup>8, a</sup>, Randall V. Martin<sup>8</sup>,  
8 Katherine R. Travis<sup>9</sup>, Johnathan W. Hair<sup>9</sup>, Bruce E. Anderson<sup>9</sup>, Jack E. Dibb<sup>10</sup>, Jose L.  
9 Jimenez<sup>11</sup>, Pedro Campuzano-Jost<sup>11</sup>, Benjamin A. Nault<sup>11, b</sup>, Jung-Hun Woo<sup>12</sup>, Younha Kim<sup>13</sup>,  
10 Qiang Zhang<sup>14</sup>, Hong Liao<sup>15</sup>

11 <sup>1</sup>Harvard John A. Paulson School of Engineering and Applied Sciences, Harvard University, Cambridge, MA, USA

12 <sup>2</sup>Department of Atmospheric Sciences, Yonsei University, Seoul, Republic of Korea

13 <sup>3</sup>Samsung Particulate Matter Research Institute, Samsung Advanced Institute of Technology, 130 Samsung-ro,  
14 Yeongtong-gu, Suwon-si, Gyeonggi-do, Republic of Korea

15 <sup>4</sup>School of Earth and Environmental Sciences, Seoul National University, Seoul, Republic of Korea

16 <sup>5</sup>School of Energy and Environment, City University of Hong Kong, Hong Kong SAR, China

17 <sup>6</sup>School of Earth and Atmospheric Sciences, Georgia Institute of Technology, Atlanta, GA, USA

18 <sup>7</sup>Atmospheric Sciences Research Center, University at Albany, Albany, New York, USA

19 <sup>8</sup>Department of Energy, Environmental & Chemical Engineering, Washington University in St Louis, MO, USA

20 <sup>9</sup>NASA Langley Research Center, Hampton, VA, USA

21 <sup>10</sup>Institute for the Study of Earth, Oceans, and Space, University of New Hampshire, Durham, NH, USA

22 <sup>11</sup>Department of Chemistry, and Cooperative Institute for Research in Environmental Sciences, University of  
23 Colorado, Boulder, CO, USA

24 <sup>12</sup>Department of Civil and Environmental Engineering, Konkuk University, Seoul, Republic of Korea

25 <sup>13</sup>International Institute for Applied Systems Analysis (IIASA), 2361 Laxenburg, Austria

26 <sup>14</sup>Department of Earth System Science, Tsinghua University, Beijing, China.

27 <sup>15</sup>Jiangsu Key Laboratory of Atmospheric Environment Monitoring and Pollution Control, Collaborative Innovation  
28 Center of Atmospheric Environment and Equipment Technology, School of Environmental Science and  
29 Engineering, Nanjing University of Information Science and Technology, Nanjing, China.

30 <sup>a</sup> Now at Department of Atmospheric & Oceanic Sciences, University of California, Los Angeles, California, USA

31 <sup>b</sup> Now at Center for Aerosol and Cloud Chemistry, Aerodyne Research, Inc., Billerica, MA, USA

32 *Correspondence:* Shixian Zhai (zhaisx@g.harvard.edu)

33



34 **Abstract.** Geostationary satellite sensors over East Asia (GOCI and AHI) are now providing continuous mapping of  
35 aerosol optical depth (AOD) at 550 nm to improve monitoring of fine particulate matter (PM<sub>2.5</sub>) air quality. Here we  
36 evaluate our understanding of the physical relationships between AOD and PM<sub>2.5</sub> over East Asia by using the  
37 GEOS-Chem atmospheric chemistry model to simulate observations from multiple sources: 1) the joint NASA-  
38 NIER Korea - United States Air Quality aircraft campaign over South Korea (KORUS-AQ; May-June 2016); 2)  
39 AODs from the AERONET ground-based network; 3) AOD from a new GOCI/AHI fused product; and 4) surface  
40 PM<sub>2.5</sub> networks in South Korea and China. The KORUS-AQ data show that 550 nm AOD is mainly contributed by  
41 sulfate-nitrate-ammonium (SNA) and organic aerosols in the planetary boundary layer (PBL), despite large dust  
42 concentrations in the free troposphere, reflecting the optically effective size and the high hygroscopicity of the PBL  
43 aerosols. Although GEOS-Chem is successful in reproducing the KORUS-AQ vertical profiles of aerosol mass, its  
44 ability to link AOD to PM<sub>2.5</sub> is limited by under-accounting of coarse PM and by a large overestimate of nighttime  
45 PM<sub>2.5</sub> nitrate. A broader analysis of the GOCI/AHI AOD data over East Asia in different seasons shows agreement  
46 with AERONET AODs and a spatial distribution consistent with surface PM<sub>2.5</sub> network data. The AOD observations  
47 over North China show a summer maximum and winter minimum, opposite in phase to surface PM<sub>2.5</sub>. This is due to  
48 low PBL depths compounded by high residential coal emissions in winter, and high relative humidity (RH) in  
49 summer. Seasonality of AOD and PM<sub>2.5</sub> over South Korea is much weaker, reflecting weaker variation of PBL depth  
50 and lack of residential coal emissions. Physical interpretation of the satellite AOD data in terms of surface PM<sub>2.5</sub> is  
51 sensitive to accurate information on aerosol size distributions, PBL depths, RH, the role of coarse particles, and  
52 diurnal variation of PM<sub>2.5</sub>.

## 53 1 Introduction

54 PM<sub>2.5</sub> (particulate matter with aerodynamic diameter less than 2.5 μm) in surface air is a severe public health  
55 concern in East Asia. Surface monitoring networks of PM<sub>2.5</sub> are too sparse to assess population exposure and  
56 satellite observations of aerosol optical depth (AOD) can provide a valuable complement with continuous mapping  
57 (Van Donkelaar et al., 2015). The value of satellite observations is now increasing with the advent of geostationary  
58 satellite sensors, including the Geostationary Ocean Color Imager (GOCI) launched by the Korea Aerospace  
59 Research Institute (KARI) in 2011 (Choi et al., 2016; Lee et al., 2019) and the Advanced Himawari Imager (AHI)  
60 launched by the Japan Aerospace Exploration Agency (JAXA) in 2014 (Lim et al., 2018). There is a need to better  
61 understand the physical relationships between AOD and PM<sub>2.5</sub>. Here we use the GEOS-Chem chemical transport  
62 model (CTM) to analyze and simulate the AOD-PM<sub>2.5</sub> relationships over East Asia, exploiting vertical profiles from  
63 the joint NASA-NIER Korea - United States Air Quality (KORUS-AQ) field study in May-June 2016 (Crawford et  
64 al., 2021; Peterson et al., 2019; Jordan et al., 2020) as well as GOCI/AHI geostationary satellite data compared to  
65 surface observation networks.

66 A number of past studies have used satellite AOD data to infer surface PM<sub>2.5</sub> using physical and statistical models.  
67 AOD measures aerosol extinction (scattering and absorption) integrated over the atmospheric column, so that the  
68 relationship to PM<sub>2.5</sub> depends on the vertical distribution and optical properties of aerosols. The standard geophysical



69 approach has been to use a CTM, such as GEOS-Chem, to compute the  $PM_{2.5}/AOD$  ratio (Liu et al., 2004), with  
70 recent applications correcting for CTM biases using available  $PM_{2.5}$  surface network data (Van Donkelaar et al.,  
71 2016; Hammer et al., 2020). An alternative approach is to use machine-learning algorithms to relate satellite AOD to  
72  $PM_{2.5}$  by training on the surface network data (Wei et al., 2021), and sometimes including CTM values as predictors  
73 (Di et al., 2019). Yet another approach is to assimilate the satellite-measured AODs in a CTM and correct in this  
74 manner the  $PM_{2.5}$  simulation, although this requires attribution of model AOD errors to specific model parameters  
75 (Kumar et al., 2019; Saide et al., 2014; Sekiyama et al., 2010; Cheng et al., 2019). In all of these approaches, a better  
76 understanding of the physical relationship of AOD- $PM_{2.5}$  can greatly enhance the capability to infer  $PM_{2.5}$  from  
77 AOD data.

## 78 2 Data and methods

### 79 2.1 Observations

80 We use observations over China and South Korea from multiple platforms including surface sites, aircraft, and  
81 satellites (Table 1 and 2). Surface data (Table 1) include  $PM_{2.5}$  from national observation networks in China (Zhai et  
82 al., 2019) and South Korea (Jordan et al., 2020), speciated  $PM_{2.5}$  at 7 supersites in South Korea during KORUS-AQ  
83 (Choi et al., 2019), and ground-based AODs from the AERONET network at 2 sites in North China and 10 sites in  
84 South Korea (21 sites during KORUS-AQ). We use total and fine-mode AODs at 500 nm wavelength from the  
85 AERONET Version 3 Level 2.0 database (Giles et al., 2019). The AERONET AODs at 500 nm are converted to 550  
86 nm using Ångström Exponents at 500 nm for consistency with the satellite AOD data.



87 **Table 1. Surface site observations used in this work (2016)**

Variables	Number of sites
PM <sub>2.5</sub> in North China <sup>a</sup>	117
PM <sub>2.5</sub> in South Korea <sup>b</sup>	130
PM <sub>2.5</sub> composition in South Korea (May-June 2016) <sup>c</sup>	7
AERONET total and fine mode AOD in East China <sup>d</sup>	5
AERONET total and fine mode AOD in South Korea <sup>d</sup>	10-21 <sup>e</sup>

88 <sup>a</sup> Hourly PM<sub>2.5</sub> from the China National Environmental Monitoring Centre (CNEMC; [quotsoft.net/air/](http://quotsoft.net/air/)) in North  
89 China (115.5-122° E, 34.5-40.5° N), including only sites with more than 90% data coverage in each month of 2016.  
90 Quality control of the CNEMC dataset is described in our previous study (Zhai et al., 2019). The PM<sub>2.5</sub>  
91 measurements are made at reference RH ≤ 35%.

92 <sup>b</sup> Hourly PM<sub>2.5</sub> from the AirKorea network ([airkorea.or.kr](http://airkorea.or.kr)), with the same data selection criteria as for North China.  
93 The PM<sub>2.5</sub> measurements are made at reference RH ≤ 35%.

94 <sup>c</sup> Major PM<sub>2.5</sub> components including sulfate, nitrate, ammonium, organic carbon, and black carbon at 7 supersites in  
95 South Korea during KORUS-AQ (May-June 2016; Choi et al., 2019). The mass concentration of organic carbon is  
96 converted to that of organic aerosol with a multiplicative factor of 1.8 based on KORUS-AQ observations (Kim et  
97 al., 2018).

98 <sup>d</sup> AODs are from the AERONET Version 3 Level 2.0 all-points database ([aeronet.gsfc.nasa.gov](http://aeronet.gsfc.nasa.gov)), except that AODs  
99 at the XuZhou site in East China are from the Version 3 Level 1.5 database. AOD at 500 nm (AOD<sub>500nm</sub>) is  
100 converted to 550 nm (AOD<sub>550nm</sub>) using Ångström Exponent at 500 nm (AE<sub>500nm</sub>) following: AOD<sub>550nm</sub> =  
101 AOD<sub>500nm</sub>  $\left(\frac{550}{500}\right)^{-AE_{500nm}}$ .

102 <sup>e</sup> AERONET AODs in South Korea are from 10 sites for the full year of 2016 and 21 sites during KORUS-AQ.

103 The KORUS-AQ campaign (Table 2) includes 20 flights over the Korean peninsula and the surrounding ocean from  
104 May 2 to June 10, 2016, with vertical profiling up to 8 km altitude. We use the aircraft observations of remote and in  
105 situ aerosol extinction (scattering + absorption) coefficients, dry aerosol number size distributions, sub-micron non-  
106 refractory aerosol composition, bulk aerosol ionic composition, black carbon (BC), and relative humidity (RH).

107 Geostationary satellite AOD data are from the GOCI and AHI instruments, covering eastern China and South Korea  
108 at 6 km × 6 km spatial resolution and hourly temporal resolution for 8 hours per day (09:30 to 16:30 local time). We  
109 use the fused AOD product generated from the GOCI and AHI AOD retrievals, each using two different surface  
110 reflectance methods (Lim et al., 2020). Fusion of this four-member ensemble is done by the maximum likelihood  
111 estimate (MLE) method, with weighting and averaging based on errors determined by comparison to AERONET  
112 AOD. The fused satellite AOD product is shown by Lim et al. (2020) to have higher accuracy than its member  
113 products in comparison with AERONET data during the KORUS-AQ campaign. We will refer to it as the ‘GEO  
114 satellite AOD’ product in what follows.



115 **Table 2. KORUS-AQ aircraft observations used in this work (May-June 2016).**

Variables	Instruments
Aerosol extinction profile at 532 nm	HSRL <sup>a</sup>
Aerosol scattering coefficient at 550 nm	TSI nephelometers <sup>b</sup>
Aerosol absorption coefficient at 532 nm	PSAPs <sup>c</sup>
Aerosol dry size distribution	TSI LAS <sup>d</sup>
Bulk aerosol ionic composition	SAGA <sup>e</sup>
Sub-micron non-refractory aerosol composition	HR-ToF-AMS <sup>f</sup>
Black carbon concentration	HDSP2 <sup>g</sup>
Relative humidity	DLH <sup>h</sup>

116 <sup>a</sup> NASA Langley airborne High Spectral Resolution Lidar (HSRL) (Hair et al., 2008; Scarino et al., 2014).

117 <sup>b</sup> NASA Langley TSI-3563 nephelometers (Ziemba et al., 2013).

118 <sup>c</sup> Radiance Research 3-wavelength particle soot absorption photometers (PSAPs; Ziemba et al., 2013).

119 <sup>d</sup> Optical size distribution over the 0.1-5.0  $\mu\text{m}$  diameter range from the TSI Laser Aerosol Spectrometer (LAS)  
120 Model 3340. Here we follow Nault et al. (2018) and Saide et al. (2020) and multiply the LAS optical equivalent  
121 diameters by 1.115 to approximate the geometric diameter.

122 <sup>e</sup> University of New Hampshire (UNH) Soluble Acidic Gases and Aerosol (SAGA) instrument (Dibb et al., 2003).  
123 The cutoff aerodynamic diameter of the inlet is around 4  $\mu\text{m}$ , corresponding to a geometric particle diameter of 2.5  
124  $\mu\text{m}$  (Mcnaughton et al., 2007; Mcnaughton et al., 2009).

125 <sup>f</sup> University of Colorado Boulder High-Resolution Time-of-Flight Aerosol Mass Spectrometer (HR-ToF-AMS;  
126 DeCarlo et al., 2006; Nault et al., 2018; Guo et al., 2020).

127 <sup>g</sup> NOAA Humidified-Dual-Single-Particle Soot Photometer (HDSP2; Lamb et al., 2018).

128 <sup>h</sup> NASA Diode Laser Hygrometer (DLH; Podolske et al., 2003).

## 129 **2.2 GEOS-Chem simulation**

130 We use GEOS-Chem version 12.7.1 (DOI: 10.5281/zenodo.3676008) in a nested-grid simulation at a horizontal  
131 resolution of  $0.5^\circ \times 0.625^\circ$  over East Asia ( $100\text{-}145^\circ\text{E}$ ,  $20\text{-}50^\circ\text{N}$ ). GEOS-Chem simulates detailed tropospheric  
132 oxidant-aerosol chemistry and is driven here by GEOS-FP assimilated meteorological data from the NASA Global  
133 Modeling and Assimilation Office (GMAO). Boundary layer mixing uses the non-local scheme implemented by Lin  
134 and McElroy (2010). Dry deposition of gases and particles follows a standard resistance-in-series scheme (Zhang et  
135 al., 2001; Fairlie et al., 2007; Fisher et al., 2011; Jaeglé et al., 2018). Wet deposition of gases and particles includes  
136 contributions from rainout, washout, and scavenging in convective updrafts (Liu et al., 2001; Amos et al., 2012; Q.  
137 Wang et al., 2011; Q. Wang et al., 2014) with recent updates by Luo et al. (2019, 2020). We use pre-archived initial



138 conditions from Zhai et al. (2021) and run the model from December 1, 2015 to December 31, 2016. The first month  
139 is used for spin-up and the year 2016 is used for analysis.

140 GEOS-Chem has been used extensively to simulate PM<sub>2.5</sub> and its composition in East Asia (Geng et al., 2017; Li et  
141 al., 2016; Choi et al., 2019; Jeong et al., 2008; Park et al., 2021; Zhai et al., 2021). Here we use the bulk  
142 representation of aerosols including sulfate (Park Rokjin et al., 2004; Alexander et al., 2009), nitrate (Jaeglé et al.,  
143 2018), primary and secondary organics (Pai et al., 2020), BC (Q. Wang et al., 2014), natural dust in four advected  
144 size ranges (Fairlie et al., 2007), anthropogenic fine dust (Philip et al., 2017), and sea salt in two size ranges (Jaeglé  
145 et al., 2011). Heterogeneous sulfate formation on aqueous aerosols is represented by a simplified parameterization  
146 scheme (Y. Wang et al., 2014), where the SO<sub>2</sub> uptake coefficient ( $\gamma$ ) linearly increases from  $1 \times 10^{-5}$  at RH  $\leq$  50% to  
147  $2 \times 10^{-5}$  at RH = 100%. The thermodynamic equilibrium of sulfate-nitrate-ammonium (SNA) aerosols with the gas  
148 phase is computed with ISORROPIA II (Fountoukis and Nenes, 2007; Pye et al., 2009) assuming an aqueous  
149 aerosol. We include reactive uptake on dust of acid gases (HNO<sub>3</sub>, SO<sub>2</sub>, and H<sub>2</sub>SO<sub>4</sub>), limited by consumption of dust  
150 alkalinity (Fairlie et al., 2010). The alkalinity of emitted dust is estimated by assuming 7.1% Ca<sup>2+</sup> and 1.1% Mg<sup>2+</sup> as  
151 alkaline cations by dust mass (Shah et al., 2020).

152 Monthly anthropogenic emissions are from the Multi-resolution Emission Inventory in 2016 for China (MEIC;  
153 Zheng et al., 2018; <http://meicmodel.org>) and from the KORUSv5 emission inventory at base year 2015 (Woo et al.,  
154 2020; [http://aisl.konkuk.ac.kr/#/emission\\_data/korus-aq\\_emissions](http://aisl.konkuk.ac.kr/#/emission_data/korus-aq_emissions)) for other Asian countries and shipping  
155 emissions. MEIC over China applies weekly and diurnal scaling factors for all anthropogenic emissions (Zheng et  
156 al., 2018). The KORUSv5 agricultural NH<sub>3</sub> emissions apply the diurnal scaling factors from MEIC. Natural  
157 emissions include NO<sub>x</sub> from lightning (Murray et al., 2012) and soil (Hudman et al., 2012), MEGANv2 biogenic  
158 volatile organic compounds (VOCs) (Guenther et al., 2012), dust (Meng et al., 2020), and sea salt (Jaeglé et al.,  
159 2011). Open fire emissions are from the Global Fire Emissions Database version 4 (GFED4; van der Werf et al.,  
160 2017).

### 161 **2.3 AOD simulation**

162 AOD in GEOS-Chem is diagnosed by integrating vertically the aerosol scattering and absorption coefficients  
163 obtained with a standard Mie calculation applied to assumed size distributions, hygroscopicity, refractive indices,  
164 and densities for individual aerosol components, and summing over all components (Martin et al., 2003). Optical  
165 properties are listed in Table 3. Sulfate, nitrate, and ammonium share the same optical properties and are lumped as  
166 an SNA aerosol component for the purpose of optical calculations. All aerosol components except dust are assumed  
167 to follow log-normal size distributions. Dust includes 7 size bins (centered at radii of 0.15, 0.25, 0.4, 0.8, 1.5, 2.5,  
168 and 4.0  $\mu\text{m}$ ) for optical calculations, with the smallest four bins partitioned by mass from the first advected dust bin  
169 ( $< 2.5 \mu\text{m}$  in geometric diameter) following L. Zhang et al. (2013). Dust particles follow a gamma size distribution  
170 within their optical size bins (Curci, 2012). The BC absorption enhancement from coating is as given by X. Wang et  
171 al. (2014).



172 Our initial simulations indicated that aerosol extinction coefficients from the standard GEOS-Chem version 12.7.1  
173 underestimated in situ measured extinction coefficients during KORUS-AQ by 20% on average (Figure S1). We  
174 traced this problem to bias in the assumed size distributions for SNA and organic aerosol, as shown in Section 3  
175 (and in Supplementary text and Figure S1-S3). Therefore, we re-computed the diagnostic AOD using updated log-  
176 normal size distributions for SNA and organic aerosol with number median radius  $R_{N,med} = 0.11 \mu\text{m}$  and geometric  
177 standard deviation  $\sigma = 1.4$ , as compared to  $R_{N,med} = 0.058 \mu\text{m}$  and  $\sigma = 1.6$  in the standard model version 12.7.1.

178 **Table 3. Aerosol optical properties <sup>a</sup>.**

Aerosol component	$R_{N,med}$ , $\mu\text{m}$	$\sigma$	Hygroscopicity <sup>b</sup>	Refractive index	$\rho$ , $\text{g cm}^{-3}$
SNA <sup>c</sup>	0.11	1.4	$\kappa = 0.61$	$1.53 - 6.0 \times 10^{-3}i$	1.7
Organic <sup>c</sup>	0.11	1.4	$\kappa = 0.1$	$1.53 - 6.0 \times 10^{-3}i$	1.3
BC	0.020	1.6	GADS	$1.75 - 4.4 \times 10^{-3}i$	1.8
Sea salt (fine)	0.085	1.5	GADS	$1.5 - 1.0 \times 10^{-3}i$	2.2
Sea salt (coarse)	0.40	1.8	GADS	$1.5 - 1.0 \times 10^{-3}i$	2.2
Dust	7 size bins	NA	$\kappa = 0$ <sup>d</sup>	$1.558 - 1.4 \times 10^{-3}i$	2.5-2.65 <sup>e</sup>

179 <sup>a</sup> Aerosol optical properties used in this work for computing aerosol scattering and absorption coefficients. Values  
180 are from the standard GEOS-Chem model version 12.7.1, except for the size distributions of SNA and organic  
181 aerosol (see text). All aerosol components except dust have log-normal dry size distributions where  $R_{N,med}$  is the  
182 number median radius and  $\sigma$  is the geometric standard deviation. Refractive indices are for 550 nm wavelength.  $\rho$  is  
183 the dry aerosol mass density.

184 <sup>b</sup> Hygroscopic growth for SNA and organic aerosol as a function of relative humidity (RH, %) is computed from  $\kappa$ -  
185 Kohler theory as a diameter growth factor  $GF = (1 + \kappa * RH/(100-RH))^{1/3}$  (Latimer and Martin, 2019). Hygroscopic  
186 growth factors for other aerosol components are from the Global Aerosol Data Set (GADS) as tabulated in Chin et  
187 al. (2002) and Martin et al. (2003).

188 <sup>c</sup>  $R_{N,med}$  and  $\sigma$  are fit to KORUS-AQ observations as described in the text. Standard GEOS-Chem v12.7.1 assumes  
189  $R_{N,med} = 0.058 \mu\text{m}$ ,  $\sigma = 1.6$  (Latimer and Martin, 2019).

190 <sup>d</sup> Hygroscopic growth of dust particles is assumed negligible.

191 <sup>e</sup> Sub-micron dust particles have a density of  $2.5 \text{ g cm}^{-3}$  while coarse mode dust particles have a density of  $2.65 \text{ g}$   
192  $\text{cm}^{-3}$ . Dust size distribution is described in the text.

### 193 **3 Aerosol concentrations and optical properties during KORUS-AQ**

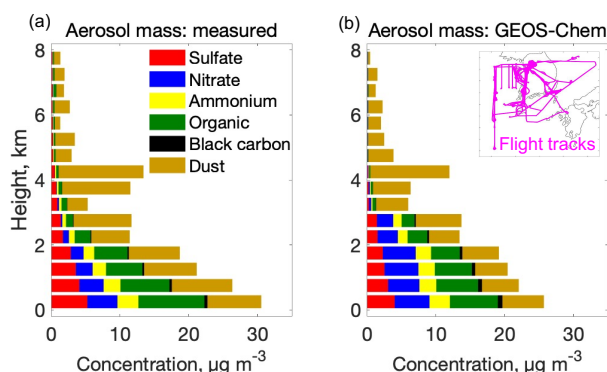
194 Here we use the KORUS-AQ aircraft observations and their simulation with GEOS-Chem to better understand the  
195 vertical distributions of different aerosol components contributing to AOD over South Korea. We begin with the  
196 mean vertical profile of aerosol mass and go on to examine the aerosol optical properties. This provides the basis for  
197 analyzing the observed vertical profile of aerosol extinction, its simulation by GEOS-Chem, and the consistency  
198 with GEO satellite and AERONET AOD measurements over South Korea during the KORUS-AQ period.



### 199 3.1 Vertical profile of aerosol mass

200 Figure 1 shows the mean vertical profiles of aerosol mass observed during KORUS-AQ and their simulation by  
201 GEOS-Chem. Here and elsewhere, the model is sampled along the flight tracks and at the flight times. The observed  
202 vertical distribution of aerosol mass concentrations (Figure 1a) shows that 58% of column aerosol mass is below 2  
203 km altitude, which we define as the planetary boundary layer (PBL), and 34% is at 2-5 km altitude, which we define  
204 as the lower free troposphere (FT). The model has a similar vertical distribution (Figure 1b), with 57% of aerosol  
205 mass in the PBL and 36% in the lower FT. SNA, organic, and dust each contribute about a third of aerosol mass in  
206 the PBL while dust dominates in the lower FT both in the observations and in the model. The enhanced dust in the  
207 lower FT is driven by a few dust events, which the model reproduces (Figure S2). Black carbon and sea salt (not  
208 shown) make only minor contributions to aerosol mass. The model underestimates sulfate by 28% in the PBL, which  
209 leads to a 20% overestimate of nitrate, with canceling effect on the SNA mass simulation.

210 The GEOS-Chem simulation of organic aerosol in this work uses the simple scheme of Pai et al. (2020) and  
211 underestimates aircraft observations by 16% in the PBL. Over 90% of GEOS-Chem organic aerosol is secondary,  
212 consistent with observations (Figure S4; Nault et al., 2018; Pai et al., 2020). GEOS-Chem simulation of the  
213 KORUS-AQ aerosol component profiles for different meteorological regimes is presented in Park et al. (2021).



214

215 **Figure 1. Vertical profiles of aerosol mass during KORUS-AQ. Panel (a) shows the mean vertical distributions of**  
216 **observed mass concentrations of major aerosol components at ambient temperature and pressure. Panel (b) is the same as**  
217 **(a) but from the GEOS-Chem model sampled along the flight tracks (inset). We derive dust concentration from SAGA**  
218 **Ca<sup>2+</sup> and Na<sup>+</sup> following Shah et al. (2020) by assuming that non-sea salt Ca<sup>2+</sup> accounts for 7.1% of dust mass: [dust] =**  
219 **([Ca<sup>2+</sup>] - 0.0439 [Na<sup>+</sup>]/2) / 0.071 where the brackets denote mass concentration. Modeled dust is shown for particles with**  
220 **geometric diameter < 2.5 µm, to be consistent with SAGA measurements (Table 2 footnote e). Measured sulfate, nitrate,**  
221 **ammonium, and organic aerosol concentrations are from the AMS instrument (values from the SAGA instrument are**  
222 **shown in Figure S4). All data are averaged over 500-m vertical bins. Here and elsewhere, we excluded pollution plumes**  
223 **diagnosed by either NO<sub>2</sub> or SO<sub>2</sub> > 10 ppbv (3.4% of all the data).**





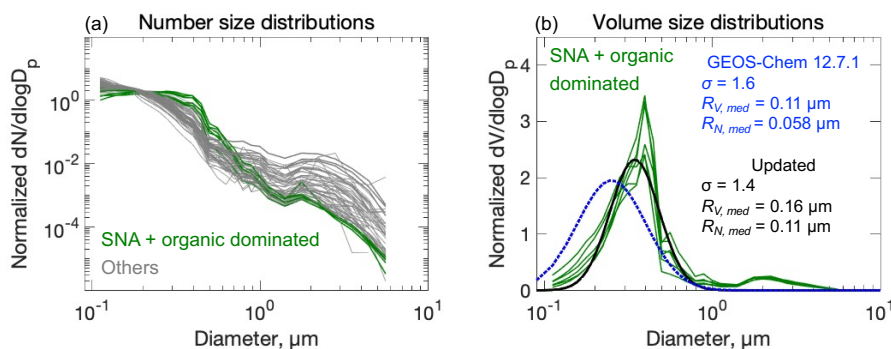
### 224 3.2 Aerosol size distributions

225 Figure 2a shows the normalized dry aerosol number size distributions on each of the 20 flights and in 3 altitude  
226 bands: < 1.5 km, 3-5 km, and 6-7 km (60 lines). The spread in the size distributions above 1  $\mu\text{m}$  in diameter reflects  
227 dust influence. We select measurements below 1.5 km altitude when SNA + organic aerosol mass concentrations are  
228 more than 4 times that of dust as defining the SNA + organic aerosol size distributions (green lines in Figure 2a).  
229 Conditions dominated by SNA + organic aerosols define the lower envelopes of the ensemble of size distributions at  
230 diameter > 1  $\mu\text{m}$ . SNA and organics were observed to have similar size distributions during KORUS-AQ (Kim et  
231 al., 2018).

232 Figure 2b converts the SNA + organic dominated number size distributions to volume size distributions. The  
233 observed SNA + organic dominated aerosol size distribution is shifted toward larger sizes relative to the standard  
234 GEOS-Chem. The secondary maximum in the coarse mode could be due to dust. We fitted the observed SNA +  
235 organic aerosol size distributions to a lognormal distribution with volume median radius  $R_{V,med} = 0.16 \mu\text{m}$  and  
236 geometric standard deviation  $\sigma = 1.4$ . The number median radius is derived from the volume median radius  
237 following Seinfeld and Pandis (2016):

$$238 \ln R_{N,med} = \ln R_{V,med} - 3\ln^2\sigma \quad (1)$$

239 which yields  $R_{N,med} = 0.11 \mu\text{m}$ . In comparison, the standard GEOS-Chem size distribution from Latimer and Martin  
240 (2019) has  $R_{N,med} = 0.058 \mu\text{m}$  and  $\sigma = 1.6$ . We adopt the observed log-normal size distribution parameters in what  
241 follows (Table 3).



242  
243 **Figure 2.** Aerosol dry size distributions measured in the KORUS-AQ aircraft campaign. Panel (a) shows mean  
244 normalized number size distributions measured on each of the 20 flights and for 3 altitude bins: < 1.5 km, 3-5 km, and 6-7  
245 km (60 lines total). The SNA + organic dominated size distribution profiles are highlighted in color. Panel (b) shows  
246 normalized volume size distributions for conditions dominated by SNA + organic aerosols (green lines), along with a least-  
247 square fit to a lognormal distribution (black line), and the standard GEOS-Chem v12.7.1 size distribution from Latimer  
248 and Martin (2019) (blue dashed line). Normalization imposes an arbitrary value of unit area below each line. Lognormal  
249 distribution parameters are inset in panel (b) including volume median radius ( $R_{V,med}$ ), number median radius ( $R_{N,med}$ ),  
250 and geometric standard deviation ( $\sigma$ ).

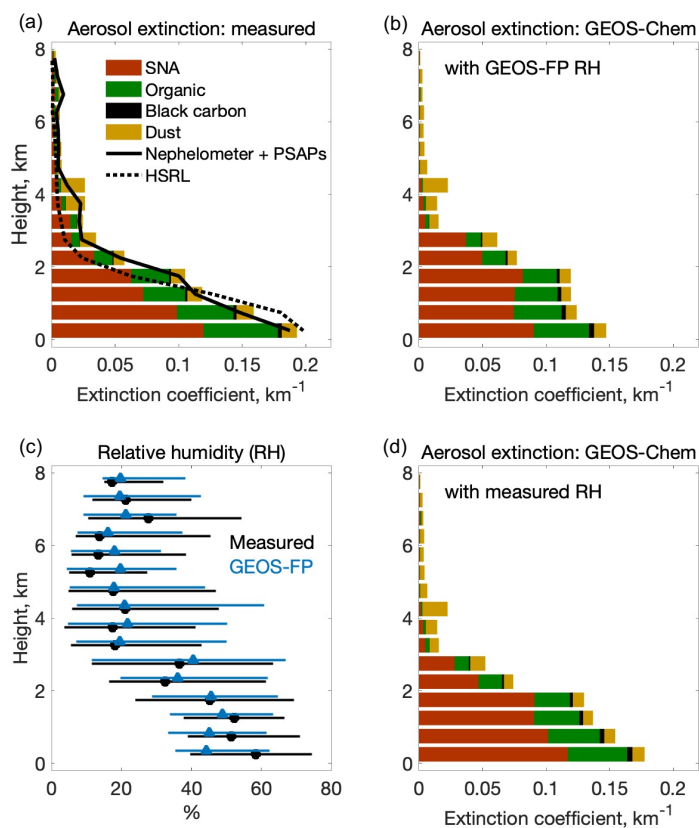


251 **3.3 Aerosol extinction and relation to AOD**

252 Figure 3 shows the vertical profiles of ambient aerosol extinction coefficients and RH during KORUS-AQ. Vertical  
253 profiles of aerosol extinction were measured on the aircraft both remotely with the HSRL instrument (above and  
254 below the aircraft) and in situ with TSI-3563 nephelometers (for scattering) and PSAPs (for absorption). The two  
255 agree well, as shown in Figure 3a. They indicate that 76-90% of column aerosol extinction is in the PBL at 0-2 km  
256 altitude and 9-19% is in the lower FT at 2-5 km. Both measurements show that aerosol extinction is much more  
257 strongly weighted to the PBL than aerosol mass (Figure 1).

258 Also shown in Figure 3a are the contributions of individual aerosol components to the extinction profile, as  
259 computed from the GEOS-Chem optical properties (Table 3) applied to the observed mass concentrations. The sum  
260 shows a good match to the measured extinction coefficient profiles. The much larger contribution of the PBL to  
261 column aerosol extinction than to column mass is because aerosol mass in the lower FT is mainly composed of dust,  
262 whose mass extinction efficiency is much smaller than SNA and organics due to its coarse size and lack of  
263 hygroscopic growth (Figure S5). The mean AOD inferred from the aircraft data is 0.36 and is contributed 59% by  
264 SNA, 27% by organic aerosol, 12% by dust, and 2% by BC. It is consistent with the mean AODs measured at  
265 AERONET stations in South Korea during KORUS-AQ (Figure S6).

266 Figure 3b shows the GEOS-Chem simulation of aerosol extinction profiles for comparison to the observations in  
267 Figure 3a. The model underestimates extinction coefficients by 20% below 1 km altitude, although there is no such  
268 underestimate in aerosol mass. This is caused by a negative RH bias in the GEOS-FP meteorological data used to  
269 drive GEOS-Chem, particularly at high RH conditions (Figure 3c) and is corrected if we apply the observed RH  
270 rather than the GEOS-FP RH to the GEOS-Chem aerosol mass concentrations (Figure 3d).



271  
272 **Figure 3.** Vertical profiles of aerosol extinction coefficients and relative humidity (RH) during KORUS-AQ. Panel (a)  
273 shows the mean observed vertical distributions of 550 nm extinction coefficients measured in situ (nephelometer + PSAPs);  
274 at ambient RH) and remotely (HSRL), along with an independent calculation (colored horizontal bars) from the  
275 measured mass concentrations of major aerosol components, measured RH, and GEOS-Chem optical properties as given  
276 in Table 3. Panel (b) shows the mean aerosol extinction profile in GEOS-Chem and the contributions from the different  
277 model components. Panel (c) is the median vertical profile of RH (horizontal bars are 25-75<sup>th</sup> percentiles) from aircraft  
278 measurements and the GEOS-FP assimilated meteorological data used to drive GEOS-Chem. Panel (d) is the same as (b)  
279 but calculated using measured RH.

#### 280 4 AOD and surface particulate matter over South Korea during KORUS-AQ

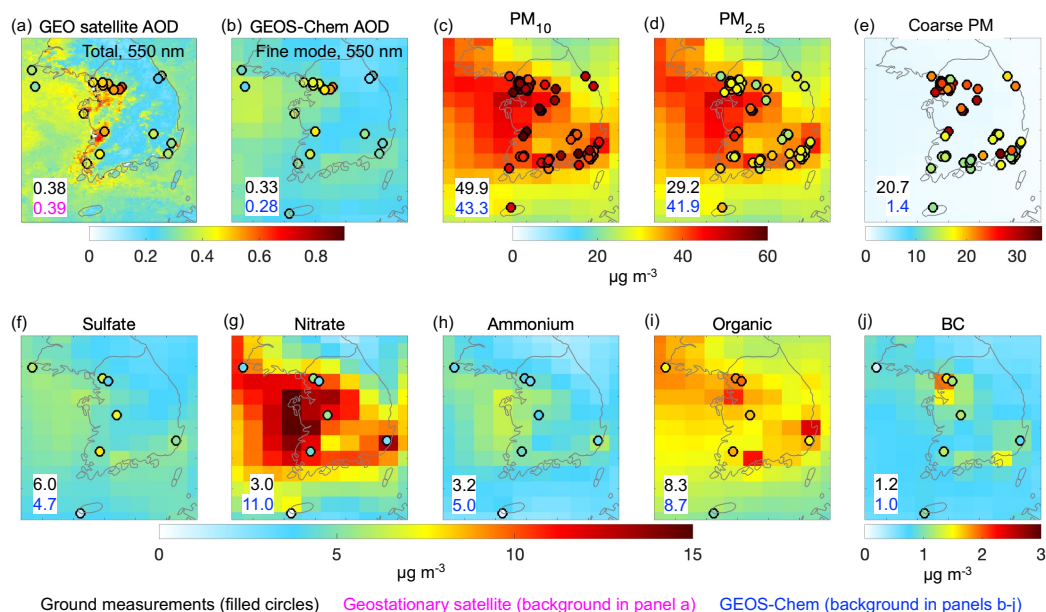
281 Our analysis of Section 3 used the KORUS-AQ aircraft data to attribute AOD over South Korea to individual  
282 aerosol components and altitudes. We now take the next step of relating satellite to AERONET AODs over the  
283 Korea peninsula during KORUS-AQ and evaluating the capability of GEOS-Chem to simulate observed AODs and  
284 surface particulate matter concentrations.



285 Figure 4a shows the spatial distribution of the fused geostationary satellite (GOCI/AHI) AOD (GEO satellite AOD)  
286 during the KORUS-AQ period with AERONET AOD added as circles. The GEO satellite AOD shows high values  
287 (0.5-0.6) along the west coast of South Korea, significantly correlated with AERONET total AOD with a spatial  
288 correlation coefficient ( $r$ ) of 0.7. GEO satellite AOD is biased low at sites in the Seoul Metropolitan Area (SMA)  
289 and is biased high on the Yellow Sea islands, resulting in an overall -10% bias, consistent with the validation by Lim  
290 et al. (2020). Sampling the AODs at or near the seven PM<sub>2.5</sub> supersites operating during KORUS-AQ shows no  
291 significant bias (inset values in Figure 4a).

292 Figure 4b-e shows the spatial distributions of GEOS-Chem AOD, surface PM<sub>10</sub> (particulate matter with aerodynamic  
293 diameter less than 10  $\mu\text{m}$ ), surface PM<sub>2.5</sub>, and surface coarse PM (PM<sub>10</sub> minus PM<sub>2.5</sub>; particulate matter with  
294 aerodynamic diameter less than 10  $\mu\text{m}$  and larger than 2.5  $\mu\text{m}$ ), with surface observations shown as circles and  
295 median values at the measurement sites inset. GEOS-Chem reproduces the satellite AOD enhancements along the  
296 west coast of South Korea but the values are lower than observed. Comparison of AERONET total and fine mode  
297 AOD shows a 13% contribution of coarse particles to total AOD. Comparison of GEOS-Chem to the fine-mode  
298 AERONET AOD, as shown in Figure 4b, finds a 15% underestimate that could be attributed to the low-RH bias  
299 (Figure 3c). Concurrent measurements of PM<sub>10</sub> and PM<sub>2.5</sub> at AirKorea sites show that coarse PM (median 21  $\mu\text{g m}^{-3}$ )  
300 accounts for 41% of total PM<sub>10</sub> (50  $\mu\text{g m}^{-3}$ ), while coarse PM in GEOS-Chem is much lower (1.4  $\mu\text{g m}^{-3}$ ; Figure 4e).  
301 Therefore, the GEOS-Chem underestimate of AOD can mostly be attributed to missing coarse PM. Coarse PM has a  
302 concentration larger than 10  $\mu\text{g m}^{-3}$  across South Korea, with higher concentration in the SMA ( $\sim 30 \mu\text{g m}^{-3}$ ) than in  
303 rural areas ( $\sim 15 \mu\text{g m}^{-3}$ ), implying an origin from both anthropogenic and natural sources (Figure 4e).

304 GEOS-Chem overestimates surface PM<sub>2.5</sub> by 43% over South Korea (Figure 4d), in contrast to the simulation of  
305 AERONET fine mode AOD (Figure 4b). Figure 4f-j shows the spatial distributions of major PM<sub>2.5</sub> components in  
306 GEOS-Chem (background) and measurements (filled circles). GEOS-Chem is not significantly biased relative to the  
307 observations for organic aerosol and BC, and underestimates sulfate by 22%. We find that the model bias for PM<sub>2.5</sub>  
308 is largely driven by nitrate, which is overestimated by a factor of 3 and leads to an 56% overestimate of ammonium.  
309 By contrast, comparison to the KORUS-AQ data below 1-km altitude showed only a 20% overestimate of nitrate  
310 (Figure 1). This is because the model bias is mainly driven by nighttime conditions, as shown in Figure 5. The cause  
311 of this large model bias is analyzed by K. R. Travis et al. (manuscript in preparation) and attributed to nighttime  
312 nitrate chemistry in the stratified boundary layer.



313

314

315

316

317

318

319

320

321

322

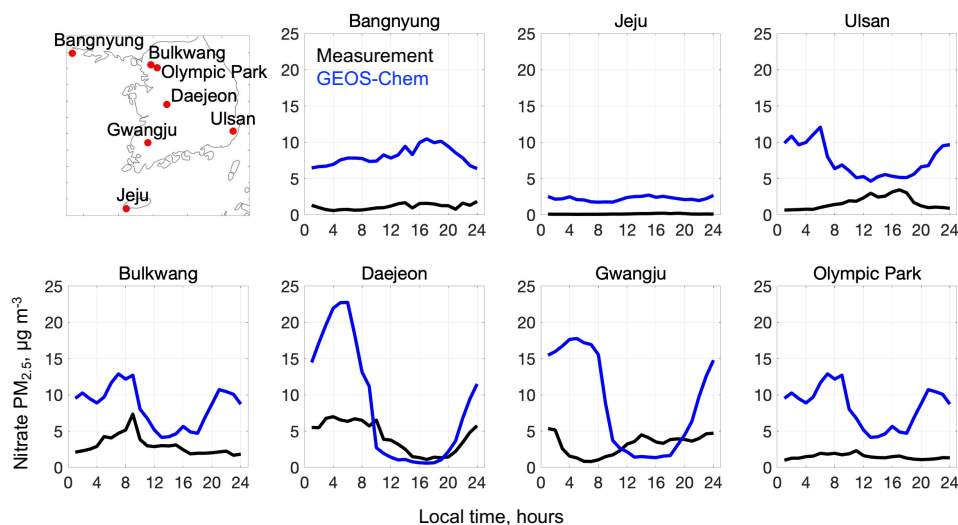
323

324

325

326

Figure 4. Spatial distributions of AOD, surface  $PM_{10}$ ,  $PM_{2.5}$ , coarse PM ( $PM_{10}$  minus  $PM_{2.5}$ ), and major  $PM_{2.5}$  components over South Korea averaged during KORUS-AQ (May 9 - June 10, 2016). Panel (a) shows the fused geostationary (GEO) 550 nm AOD from the GOCI and AHI satellites (background) and AERONET 550 nm total AOD (filled circles). Panel (b) shows GEOS-Chem 550 nm AOD sampled at hourly GEO satellite AOD (GEOS-Chem clear-sky AOD; background) and AERONET 550 nm fine mode AOD (filled circles). Panel (c) shows surface  $PM_{10}$  modelled by GEOS-Chem (background) and measured at ground sites (filled circles). Panels (d-j) are the same as panel (c) but respectively for  $PM_{2.5}$ , coarse PM ( $PM_{10}$  minus  $PM_{2.5}$ ), and sulfate, nitrate, ammonium, organic, and BC  $PM_{2.5}$  components. Values inset are median values from ground-based measurements (black) and sampled from GEO satellite (magenta) and GEOS-Chem (blue). Measured  $PM_{10}$ ,  $PM_{2.5}$ , and coarse PM in panels (c-e) are shown for a random selection of 50% of AirKorea sites to visualize spatial distribution, and inset values are for the seven supersites where  $PM_{2.5}$  composition was measured. Median AOD values inset are sampled at or near the seven supersites to avoid biasing by the large number of sites in the Seoul Metropolitan Area. Modelled total  $PM_{2.5}$  concentrations are calculated at 35% RH (Table 3). Modelled  $PM_{10}$  is the sum of  $PM_{2.5}$ , coarse dust, and coarse sea salt.



327  
328 **Figure 5. Median diurnal variations of PM<sub>2.5</sub> nitrate concentrations at the seven supersites (top left panel) operated in**  
329 **South Korea during KORUS-AQ (May 9 - June 10, 2016). Values are medians binned by hour. GEOS-Chem model**  
330 **values are sampled to coincide with the measurements.**

## 331 **5 AOD and its relationship to PM<sub>2.5</sub> over East Asia**

332 We build on our analysis of the KORUS-AQ period for a broader interpretation of the distribution of AOD over  
333 Korea and China and its relationship to surface PM<sub>2.5</sub>, acknowledging that the conditions sampled in KORUS-AQ  
334 may not be representative of other seasons or of China. Figure 6 shows the spatial distributions of 2016 annual and  
335 seasonal mean geostationary (GEO) satellite AODs, the corresponding GEOS-Chem clear-sky AODs, and GEOS-  
336 Chem surface PM<sub>2.5</sub>. The Figure gives normalized mean biases (*NMBs*) relative to ground-based measurements from  
337 AERONET and from the PM<sub>2.5</sub> surface networks (shown as circles).

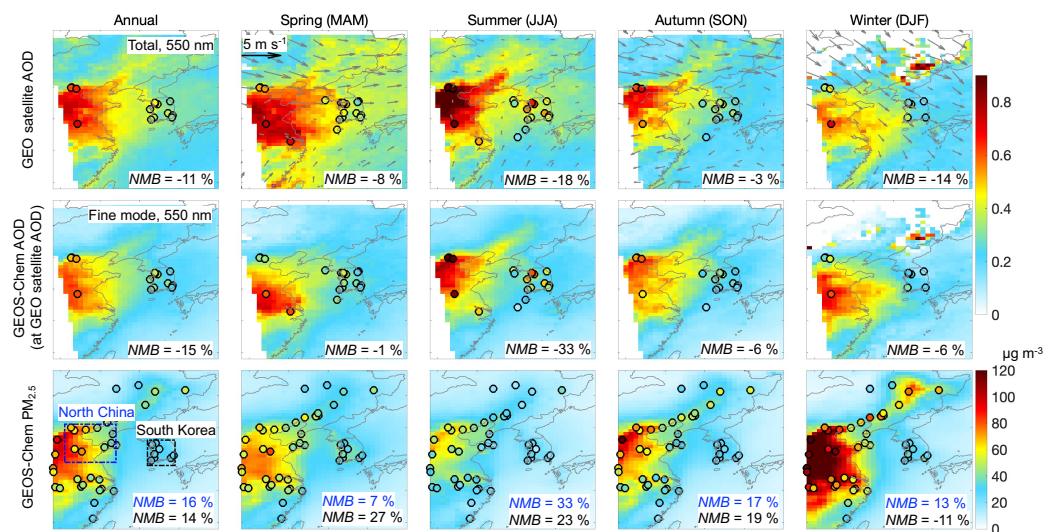
338 On an annual mean basis, AOD over North China (~ 0.5-0.6) is about 50% larger than over South Korea (~ 0.3-0.4).  
339 AOD over South Korea shows higher values (> 0.4) in the Seoul Metropolitan Area, consistent with that during the  
340 KORUS-AQ period (Figure 4a). Transport from the Asian continent is strongest in spring when the frequency of  
341 cold front passages is highest (Liu et al., 2003). AERONET total AOD in spring (0.4-0.6) is twice as large as fine-  
342 mode AOD (0.2-0.3), reflecting a large contribution of dust. In seasons other than spring, 80-90% of AERONET  
343 total AOD is contributed by the fine mode. There is large seasonality in AODs over North China, and weaker  
344 seasonality over South Korea, which will be discussed below.

345 The GEOS-Chem clear-sky AODs show the same spatial and seasonal patterns as GEO satellite AODs but tend to  
346 be low in spring and summer. Comparison of the model to AERONET AODs confirms this bias and shows better  
347 agreement with fine-mode AOD in spring (*NMB* of -1%), implying an underestimate of coarse dust that is consistent  
348 with our comparisons to the AirKorea PM<sub>10</sub> network data (Figure 4e). Comparison of clear-sky and all-sky AODs in



349 GEOS-Chem shows no significant difference on an annual and seasonal mean basis, except for winter (Figure S7).  
350 Winter has larger all-sky AOD than clear-sky AOD and the lowest rate of successful satellite retrievals (Figure S7),  
351 which may be due in part to misclassification of heavy wintertime  $PM_{2.5}$  pollution as clouds (Zhang et al., 2020).

352 The spatial distributions of  $PM_{2.5}$  in GEOS-Chem in different seasons match closely the observations (Figure 6,  
353 bottom row). We see also a close coincidence between the spatial distributions of  $PM_{2.5}$  and AODs, both in the  
354 observations and the model. On an annual mean basis, GEOS-Chem overestimates  $PM_{2.5}$  by 16% in North China  
355 and by 14% in South Korea, even though it underestimates AERONET fine mode AODs by 15%. The overestimate  
356 of  $PM_{2.5}$  in South Korea is worst in spring (27%), consistent with KORUS-AQ results which we previously  
357 attributed to excessive nighttime nitrate build-up in the model. Over North China, the overestimate of  $PM_{2.5}$  is worst  
358 in summer (33%), consistent with the nitrate overestimate in summer shown in our previous study (Zhai et al.,  
359 2021), which could also be due to model overestimate of nighttime nitrate (Miao et al., 2020).



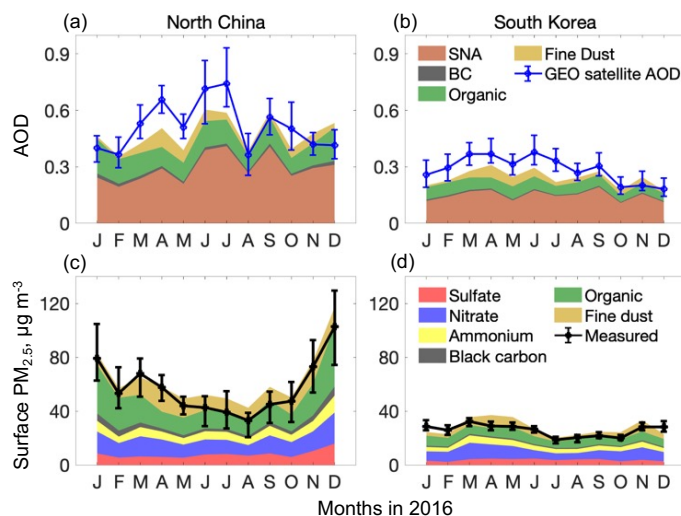
360  
361 **Figure 6. Spatial distributions of 2016 annual and seasonal mean AOD (550 nm) and surface  $PM_{2.5}$ . The top row shows**  
362 **the observed GOCI/AHI geostationary satellite AOD (GEO satellite AOD) on the GEOS-Chem  $0.5^\circ \times 0.625^\circ$  grids with**  
363 **925 hPa GEOS-FP wind fields and AERONET total AODs (circles). The middle row shows GEOS-Chem AOD sampled**  
364 **in the same way as hourly GEO satellite AOD (GEOS-Chem clear-sky AOD), with AERONET fine mode AOD added as**  
365 **circles. The bottom row shows GEOS-Chem surface  $PM_{2.5}$  (background) with surface network measurements (circles).**  
366 **AERONET AODs are shown only when more than 10 months of data are available for the annual mean and all 3 months**  
367 **data are available for each season. The  $PM_{2.5}$  observations shown are for a random selection of 7% of network sites for**  
368 **visual clarity. GEOS-Chem  $PM_{2.5}$  is calculated at 35% RH (Table 3). Normalized mean biases (NMBs) inset are for the**  
369 **comparisons of GEO satellite and GEOS-Chem values to the corresponding ground measurements.**

370 Figure 7 compares the seasonalities of AOD and  $PM_{2.5}$  over the North China and South Korea regions. The GEO  
371 satellite AOD over North China peaks in July and is minimum in winter. Most of AOD is attributed by GEOS-Chem  
372 to SNA aerosol, same as in South Korea. AOD over South Korea also has a summer maximum and winter minimum



373 but with weaker amplitude than over North China. The model is biased low in the summer and this is largely due a  
374 low RH bias (Figure S8), as seen previously in the KORUS-AQ comparisons but amplified by the high RH in  
375 summer that drives hygroscopic growth (Latimer and Martin, 2019).

376 Surface  $PM_{2.5}$  in the observations over North China and South Korea shows opposite seasonality to AOD, with  
377 minimum values in summer and maximum values in winter-spring. GEOS-Chem reproduces the strong seasonality  
378 of  $PM_{2.5}$  in North China and the much weaker seasonality in South Korea. The high  $PM_{2.5}$  values over North China  
379 in winter in the model are mostly driven by organic aerosol, reflecting the large residential coal burning source  
380 (Figure S9; Zheng et al., 2018). In South Korea, by contrast, household energy is mainly from natural gas and  
381 electricity (Lee et al., 2020; Woo et al., 2020). PBL height also shows a stronger seasonality over North China than  
382 over South Korea (Figure S8). The mean  $PM_{2.5}$ /AOD ratio over North China in winter ( $236 \mu\text{g m}^{-3}$ ) is 8 times that in  
383 summer ( $29 \mu\text{g m}^{-3}$ ), with autumn ( $94 \mu\text{g m}^{-3}$ ) and spring ( $89 \mu\text{g m}^{-3}$ ) in between, while over South Korea, the  
384  $PM_{2.5}$ /AOD ratio in winter ( $62 \mu\text{g m}^{-3}$ ) is only 70% larger than in summer ( $36 \mu\text{g m}^{-3}$ ).



385  
386 **Figure 7. Seasonality of AOD and  $PM_{2.5}$  over North China and South Korea, and contributions from individual aerosol**  
387 **components. Lines show regional medians (error bars: 25<sup>th</sup> and 75<sup>th</sup> percentiles) for the ensemble of monthly averaged**  
388 **observations in the regions (Figure 6) in 2016. GEOS-Chem values are shown as stacked contours for individual**  
389 **components and are sampled in the same way as the observations.**

## 390 6 Conclusions

391 Geostationary satellite observations of aerosol optical depth (AOD) from the GOCI and AHI satellite instruments  
392 have tremendous potential for monitoring of  $PM_{2.5}$  air quality over East Asia if they can be properly interpreted.  
393 Here we used a new fused GOCI/AHI satellite product together with AERONET ground-based AOD measurements,  
394 vertical profiles over South Korea from the KORUS-AQ aircraft campaign (May-June 2016), and surface network





395 PM observations, simulated collectively with the GEOS-Chem transport model, to better understand the physical  
396 relationship between satellite AOD and PM<sub>2.5</sub>.

397 The KORUS-AQ observations show that total aerosol extinction (550 nm) in the vertical column is dominated by  
398 sulfate-nitrate-ammonium (SNA) and organic aerosol in the planetary boundary layer (PBL), despite large  
399 concentrations of dust in the free troposphere. This reflects the 550 nm optically effective size and high  
400 hygroscopicity of the PBL aerosols. Adjustment of GEOS-Chem aerosol optical properties to the observed SNA and  
401 organic aerosol size distributions enabled a successful simulation of the aerosol extinction profile, although the  
402 simulation is highly sensitive to bias in the relative humidity (RH) of the driving meteorological data. SNA aerosol  
403 contributed 59% of column aerosol extinction in the KORUS-AQ data, while organic aerosol contributed 27% and  
404 dust contributed 12%.

405 Comparison of GOCI/AHI geostationary (GEO) satellite AOD to AERONET AODs over South Korea shows good  
406 agreement, with high values along the west coast. GEOS-Chem is more consistent with the fine-mode AERONET  
407 AOD because of its insufficient accounting of coarse particles, which account for 13% of AERONET AOD. GEOS-  
408 Chem overestimates 24-h surface PM<sub>2.5</sub> over South Korea by 43% during the KORUS-AQ period, despite its  
409 successful simulation of the aircraft data and fine-mode AERONET AOD, and we find that this is due to a large  
410 overestimate of nighttime nitrate.

411 Broader examination of the GOCI/AHI AOD satellite data over East Asia shows spatial distributions and  
412 magnitudes consistent with AERONET and featuring in particular strong Asian outflow in spring that includes a  
413 large dust component. We find that AODs and PM<sub>2.5</sub> have similar large-scale spatial distributions but opposite  
414 seasonality. PM<sub>2.5</sub> in North China has a strong winter maximum and summer minimum, while the AOD shows the  
415 opposite. We find that this is mainly driven by residential coal heating sources and low PBL depths in winter, and  
416 high RH in summer. Observations of PM<sub>2.5</sub> and AOD in South Korea show the same seasonal phases as in North  
417 China but with much weaker amplitude, reflecting the lack of residential coal burning in winter and a weaker  
418 seasonal amplitude of PBL depth.

419 In summary, we find that the geostationary GOCI/AHI satellite AOD data provide high-quality information for  
420 monitoring of PM<sub>2.5</sub> over East Asia but that physical interpretation requires accurate information on aerosol size  
421 distributions, PBL depths, RH, the role of coarse particles, and diurnal variation of PM<sub>2.5</sub>. Addressing these  
422 uncertainties should be a target of future work.

423

424 *Data availability.* Aircraft data during KORUS-AQ are available at: [www-air.larc.nasa.gov/cgi-](http://www-air.larc.nasa.gov/cgi-bin/ArcView/korusaq)  
425 [bin/ArcView/korusaq](http://bin/ArcView/korusaq). PM<sub>2.5</sub> data over China are from: [quotsoft.net/air/](http://quotsoft.net/air/). PM<sub>2.5</sub> data over South Korea are from:  
426 [www.airkorea.or.kr/web](http://www.airkorea.or.kr/web). AERONET data can be found at: [aeronet.gsfc.nasa.gov](http://aeronet.gsfc.nasa.gov). The MEIC emission inventory are



427 at: [www.meicmodel.org/](http://www.meicmodel.org/). The KORUSv5 emission inventory is developed by Konkuk University, available at:  
428 [http://aisl.konkuk.ac.kr/#/emission\\_data/korus-aq\\_emissions](http://aisl.konkuk.ac.kr/#/emission_data/korus-aq_emissions).

429

430 *Author contributions.* SZ and DJJ designed the study. SZ performed the data analysis and model simulations with  
431 contributions from JFB, KL, HCL, SKK, XW, PL, KRT, and Hong Liao. JK, SL, and Hyunkwang Lim provided  
432 satellite AOD data. RJP and JIJ contributed to AirKorea data processing. JM and RM provided the dust emission  
433 inventory. GL, FY, and JMM updated wet deposition simulation. JWH, BEA, JED, JLJ, PCJ, and BAN contributed  
434 to KORUS-AQ campaign measurements. JHW and YK provided the KORUSv5 emission inventory. QZ provided  
435 the MEIC emission inventory. SZ and DJJ wrote the paper with input from all authors.

436

437 *Acknowledgement.* This work was funded by the Samsung Advanced Institute of Technology and the Harvard-  
438 NUIST Joint Laboratory for Air Quality and Climate (JLAQC). JLJ, PCJ, and BAN acknowledge NASA grant  
439 NNX15AT96G and 80NSSC19K0124 for support.

440

441 *Competing interests.* The authors declare that they have no conflict of interest.

442

#### 443 **References**

444 Alexander, B., Park Rokjin, J., Jacob Daniel, J., and Gong, S.: Transition metal-catalyzed oxidation of atmospheric  
445 sulfur: Global implications for the sulfur budget, *J. Geophys. Res. Atmos.*, 114, D02309,  
446 <https://doi.org/10.1029/2008JD010486>, 2009.

447 Amos, H. M., Jacob, D. J., Holmes, C. D., Fisher, J. A., Wang, Q., Yantosca, R. M., Corbitt, E. S., Galarneau, E.,  
448 Rutter, A. P., Gustin, M. S., Steffen, A., Schauer, J. J., Graydon, J. A., Louis, V. L. S., Talbot, R. W., Edgerton, E.  
449 S., Zhang, Y., and Sunderland, E. M.: Gas-particle partitioning of atmospheric Hg(II) and its effect on global  
450 mercury deposition, *Atmos. Chem. Phys.*, 12, 591-603, <https://doi.org/10.5194/acp-12-591-2012>, 2012.

451 Cheng, Y., Dai, T., Goto, D., Schutgens, N. A. J., Shi, G., and Nakajima, T.: Investigating the assimilation of  
452 CALIPSO global aerosol vertical observations using a four-dimensional ensemble Kalman filter, *Atmos. Chem.*  
453 *Phys.*, 19, 13445-13467, <https://doi.org/10.5194/acp-19-13445-2019>, 2019.

454 Chin, M., Ginoux, P., Kinne, S., Torres, O., Holben, B. N., Duncan, B. N., Martin, R. V., Logan, J. A., Higurashi,  
455 A., and Nakajima, T.: Tropospheric Aerosol Optical Thickness from the GOCART Model and Comparisons with  
456 Satellite and Sun Photometer Measurements, *J. Atmos. Sci.*, 59, 461-483, [https://doi.org/10.1175/1520-0469\(2002\)059<0461:TAOTFT>2.0.CO;2](https://doi.org/10.1175/1520-0469(2002)059<0461:TAOTFT>2.0.CO;2), 2002.

458 Choi, J., Park, R. J., Lee, H.-M., Lee, S., Jo, D. S., Jeong, J. I., Henze, D. K., Woo, J.-H., Ban, S.-J., Lee, M.-D.,  
459 Lim, C.-S., Park, M.-K., Shin, H. J., Cho, S., Peterson, D., and Song, C.-K.: Impacts of local vs. trans-boundary  
460 emissions from different sectors on PM<sub>2.5</sub> exposure in South Korea during the KORUS-AQ campaign, *Atmos.*  
461 *Environ.*, 203, 196-205, <https://doi.org/10.1016/j.atmosenv.2019.02.008>, 2019.

462 Choi, M., Kim, J., Lee, J., Kim, M., Park, Y. J., Jeong, U., Kim, W., Hong, H., Holben, B., Eck, T. F., Song, C. H.,  
463 Lim, J. H., and Song, C. K.: GOCI Yonsei Aerosol Retrieval (YAER) algorithm and validation during the



- 464 DRAGON-NE Asia 2012 campaign, *Atmos. Meas. Tech.*, 9, 1377-1398, <https://doi.org/10.5194/amt-9-1377-2016>,  
465 2016.
- 466 Crawford, J. H., Ahn, J. Y., Al-Saadi, J., Chang, L., Emmons, L., Kim, J., Lee, G., Park, J. H., Park, R., Woo, J. H.,  
467 Song, C. K., Hong, J.-H., Hong, Y.-D., Lefer, B. L., Lee, M., Lee, T., Kim, S., Min, K.-E., Yum, S. S., Shin, H. J.,  
468 Kim, Y.-W., Choi, J.-S., Park, J.-S., Szykman, J. J., Long, R. W., Jordan, C. E., Simpson, I. J., Fried, A., Dibb, J. E.,  
469 Cho, S. Y., and Kim, Y. P.: The Korea-United States air quality (KORUS-AQ) field study, *Elementa-Sci. Anthropol.*,  
470 in press, 2021.
- 471 Curci, G.: FlexAOD: a chemistry-transport model post-processing tool for a flexible calculation of aerosol optical  
472 properties, 1-4, [http://pumpkin.aquila.infn.it/gabri/download/curci\\_istp2012.pdf](http://pumpkin.aquila.infn.it/gabri/download/curci_istp2012.pdf), 2012.
- 473 Di, Q., Amini, H., Shi, L., Kloog, I., Silvern, R., Kelly, J., Sabath, M. B., Choirat, C., Koutrakis, P., Lyapustin, A.,  
474 Wang, Y., Mickley, L. J., and Schwartz, J.: An ensemble-based model of PM<sub>2.5</sub> concentration across the contiguous  
475 United States with high spatiotemporal resolution, *Environ. Int.*, 130, 104909,  
476 <https://doi.org/10.1016/j.envint.2019.104909>, 2019.
- 477 Dibb, J. E., Talbot, R. W., Scheuer, E. M., Seid, G., Avery, M. A., and Singh, H. B.: Aerosol chemical composition  
478 in Asian continental outflow during the TRACE-P campaign: Comparison with PEM-West B, *J. Geophys. Res.*  
479 *Atmos.*, 108, 8815, <https://doi.org/10.1029/2002JD003111>, 2003.
- 480 Fairlie, T. D., Jacob, D. J., and Park, R. J.: The impact of transpacific transport of mineral dust in the United States,  
481 *Atmos. Environ.*, 41, 1251-1266, <https://doi.org/10.1016/j.atmosenv.2006.09.048>, 2007.
- 482 Fairlie, T. D., Jacob, D. J., Dibb, J. E., Alexander, B., Avery, M. A., van Donkelaar, A., and Zhang, L.: Impact of  
483 mineral dust on nitrate, sulfate, and ozone in transpacific Asian pollution plumes, *Atmos. Chem. Phys.*, 10, 3999-  
484 4012, <https://doi.org/10.5194/acp-10-3999-2010>, 2010.
- 485 Fisher, J. A., Jacob, D. J., Wang, Q., Bahreini, R., Carouge, C. C., Cubison, M. J., Dibb, J. E., Diehl, T., Jimenez, J.  
486 L., Leibensperger, E. M., Lu, Z., Meinders, M. B. J., Pye, H. O. T., Quinn, P. K., Sharma, S., Streets, D. G., van  
487 Donkelaar, A., and Yantosca, R. M.: Sources, distribution, and acidity of sulfate-ammonium aerosol in the Arctic in  
488 winter-spring, *Atmos. Environ.*, 45, 7301-7318, <https://doi.org/10.1016/j.atmosenv.2011.08.030>, 2011.
- 489 Fountoukis, C. and Nenes, A.: ISORROPIA II: a computationally efficient thermodynamic equilibrium model for  
490 K<sup>+</sup>-Ca<sup>2+</sup>-Mg<sup>2+</sup>-NH<sub>4</sub><sup>+</sup>-Na<sup>+</sup>-SO<sub>4</sub><sup>2-</sup>-NO<sub>3</sub><sup>-</sup>-Cl<sup>-</sup>-H<sub>2</sub>O aerosols, *Atmos. Chem. Phys.*, 7, 4639-4659,  
491 <https://doi.org/10.5194/acp-7-4639-2007>, 2007.
- 492 Geng, G., Zhang, Q., Tong, D., Li, M., Zheng, Y., Wang, S., and He, K.: Chemical composition of ambient PM<sub>2.5</sub>  
493 over China and relationship to precursor emissions during 2005-2012, *Atmos. Chem. Phys.*, 17, 9187-9203,  
494 <https://doi.org/10.5194/acp-17-9187-2017>, 2017.
- 495 Giles, D. M., Sinyuk, A., Sorokin, M. G., Schafer, J. S., Smirnov, A., Slutsker, I., Eck, T. F., Holben, B. N., Lewis,  
496 J. R., Campbell, J. R., Welton, E. J., Korkin, S. V., and Lyapustin, A. I.: Advancements in the Aerosol Robotic  
497 Network (AERONET) Version 3 database - automated near-real-time quality control algorithm with improved cloud  
498 screening for Sun photometer aerosol optical depth (AOD) measurements, *Atmos. Meas. Tech.*, 12, 169-209,  
499 <https://doi.org/10.5194/amt-12-169-2019>, 2019.
- 500 Guenther, A. B., Jiang, X., Heald, C. L., Sakulyanontvittaya, T., Duhl, T., Emmons, L. K., and Wang, X.: The  
501 Model of Emissions of Gases and Aerosols from Nature version 2.1 (MEGAN2. 1): an extended and updated  
502 framework for modeling biogenic emissions, *Geosci. Model Dev.*, 5, 1471-1492, <https://doi.org/10.5194/gmd-5-1471-2012>, 2012.
- 504 Guo, H., Campuzano-Jost, P., Nault, B. A., Day, D. A., Schroder, J. C., Dibb, J. E., Dollner, M., Weinzierl, B., and  
505 Jimenez, J. L.: The Importance of Size Ranges in Aerosol Instrument Intercomparisons: A Case Study for the ATOM  
506 Mission, *Atmos. Meas. Tech. Discuss.*, 2020, 1-49, <https://doi.org/10.5194/amt-2020-224>, 2020.
- 507 Hair, J. W., Hostetler, C. A., Cook, A. L., Harper, D. B., Ferrare, R. A., Mack, T. L., Welch, W., Izquierdo, L. R.,  
508 and Hovis, F. E.: Airborne High Spectral Resolution Lidar for profiling aerosol optical properties, *Appl. Opt.*, 47,  
509 6734-6752, <https://doi.org/10.1364/AO.47.006734>, 2008.
- 510 Hammer, M. S., van Donkelaar, A., Li, C., Lyapustin, A., Sayer, A. M., Hsu, N. C., Levy, R. C., Garay, M.,  
511 Kalashnikova, O., Kahn, R. A., Brauer, M., Apte, J. S., Henze, D. K., Zhang, L., Zhang, Q., Ford, B., Pierce, J. R.,



- 512 and Martin, R. V.: Global Estimates and Long-Term Trends of Fine Particulate Matter Concentrations (1998-2018),  
513 *Environ. Sci. Technol.*, *54*, 7879-7890, <https://dx.doi.org/10.1021/acs.est.0c01764>, 2020.
- 514 Hudman, R. C., Moore, N. E., Mebust, A. K., Martin, R. V., Russell, A. R., Valin, L. C., and Cohen, R. C.: Steps  
515 towards a mechanistic model of global soil nitric oxide emissions: implementation and space based-constraints,  
516 *Atmos. Chem. Phys.*, *12*, 7779-7795, <https://doi.org/10.5194/acp-12-7779-2012>, 2012.
- 517 Jaeglé, L., Quinn, P. K., Bates, T. S., Alexander, B., and Lin, J. T.: Global distribution of sea salt aerosols: new  
518 constraints from in situ and remote sensing observations, *Atmos. Chem. Phys.*, *11*, 3137-3157,  
519 <https://doi.org/10.5194/acp-11-3137-2011>, 2011.
- 520 Jaeglé, L., Shah, V., Thornton, J. A., Lopez-Hilfiker, F. D., Lee, B. H., McDuffie, E. E., Fibiger, D., Brown, S. S.,  
521 Veres, P., Sparks, T. L., Ebben, C. J., Wooldridge, P. J., Kenagy, H. S., Cohen, R. C., Weinheimer, A. J., Campos,  
522 T. L., Montzka, D. D., Digangi, J. P., Wolfe, G. M., Hanisco, T., Schroder, J. C., Campuzano-Jost, P., Day, D. A.,  
523 Jimenez, J. L., Sullivan, A. P., Guo, H., and Weber, R. J.: Nitrogen Oxides Emissions, Chemistry, Deposition, and  
524 Export Over the Northeast United States During the WINTER Aircraft Campaign, *J. Geophys. Res. Atmos.*, *123*,  
525 12,368-312,393, <https://doi.org/10.1029/2018JD029133>, 2018.
- 526 Jeong, J. I., Park, R. J., and Youn, D.: Effects of Siberian forest fires on air quality in East Asia during May 2003  
527 and its climate implication, *Atmos. Environ.*, *42*, 8910-8922, <https://doi.org/10.1016/j.atmosenv.2008.08.037>, 2008.
- 528 Jordan, C. E., Crawford, J. H., Beyersdorf, A. J., Eck, T. F., Halliday, H. S., Nault, B. A., Chang, L.-S., Park, J.,  
529 Park, R., and Lee, G.: Investigation of factors controlling PM<sub>2.5</sub> variability across the South Korean Peninsula during  
530 KORUS-AQ, *Elementa-Sci. Anthropol.*, *8*, 28, <https://doi.org/10.1525/elementa.424>, 2020.
- 531 Kim, H., Zhang, Q., and Heo, J.: Influence of intense secondary aerosol formation and long-range transport on  
532 aerosol chemistry and properties in the Seoul Metropolitan Area during spring time: results from KORUS-AQ,  
533 *Atmos. Chem. Phys.*, *18*, 7149-7168, <https://doi.org/10.5194/acp-18-7149-2018>, 2018.
- 534 Kumar, R., Delle Monache, L., Bresch, J., Saide, P. E., Tang, Y., Liu, Z., da Silva, A. M., Alessandrini, S., Pfister,  
535 G., Edwards, D., Lee, P., and Djalalova, I.: Toward Improving Short-Term Predictions of Fine Particulate Matter  
536 Over the United States Via Assimilation of Satellite Aerosol Optical Depth Retrievals, *J. Geophys. Res. Atmos.*,  
537 *124*, 2753-2773, <https://doi.org/10.1029/2018JD029009>, 2019.
- 538 Lamb, K. D., Perring, A. E., Samset, B., Peterson, D., Davis, S., Anderson, B. E., Beyersdorf, A., Blake, D. R.,  
539 Campuzano-Jost, P., Corr, C. A., Diskin, G. S., Kondo, Y., Moteki, N., Nault, B. A., Oh, J., Park, M., Pusede, S. E.,  
540 Simpson, I. J., Thornhill, K. L., Wisthaler, A., and Schwarz, J. P.: Estimating Source Region Influences on Black  
541 Carbon Abundance, Microphysics, and Radiative Effect Observed Over South Korea, *J. Geophys. Res. Atmos.*, *123*,  
542 13,527-513,548, <https://doi.org/10.1029/2018JD029257>, 2018.
- 543 Latimer, R. N. C. and Martin, R. V.: Interpretation of measured aerosol mass scattering efficiency over North  
544 America using a chemical transport model, *Atmos. Chem. Phys.*, *19*, 2635-2653, [https://doi.org/10.5194/acp-19-](https://doi.org/10.5194/acp-19-2635-2019)  
545 2635-2019, 2019.
- 546 Lee, S., Kim, J., Choi, M., Hong, J., Lim, H., Eck, T. F., Holben, B. N., Ahn, J.-Y., Kim, J., and Koo, J.-H.:  
547 Analysis of long-range transboundary transport (LRTT) effect on Korean aerosol pollution during the KORUS-AQ  
548 campaign, *Atmos. Environ.*, *204*, 53-67, <https://doi.org/10.1016/j.atmosenv.2019.02.020>, 2019.
- 549 Lee, W., Lim, T., and Kim, D. D.: Thermal and Energy Performance Assessment of the Prefab Electric Ondol  
550 System for Floor Heating in a Residential Building, *Energies*, *13*, 5723, <https://doi.org/10.3390/en13215723>, 2020.
- 551 Li, K., Liao, H., Zhu, J., and Moch Jonathan, M.: Implications of RCP emissions on future PM<sub>2.5</sub> air quality and  
552 direct radiative forcing over China, *J. Geophys. Res. Atmos.*, *121*, 12,985-913,008,  
553 <https://doi.org/10.1002/2016JD025623>, 2016.
- 554 Lim, H., Choi, M., Kim, J., Kasai, Y., and Chan, P.: AHI/Himawari-8 Yonsei Aerosol Retrieval (YAER):  
555 Algorithm, Validation and Merged Products, *Remote Sens.*, *10*, 699, <https://doi.org/10.3390/rs10050699>, 2018.
- 556 Lim, H., Go, S., Kim, J., Choi, M., Lee, S., Song, C. K., and Kasai, Y.: Integration of GOCI and AHI Yonsei  
557 Aerosol Optical Depth Products During the 2016 KORUS-AQ and 2018 EMerGe Campaigns, *Atmos. Meas. Tech.*  
558 *Discuss.*, 2020, 1-32, <https://doi.org/10.5194/amt-2020-336>, 2020.



- 559 Lin, J. and McElroy, M. B.: Impacts of boundary layer mixing on pollutant vertical profiles in the lower  
560 troposphere: Implications to satellite remote sensing, *Atmos. Environ.*, 44, 1726-1739,  
561 <https://doi.org/10.1016/j.atmosenv.2010.02.009>, 2010.
- 562 Liu, H., Jacob, D. J., Bey, I., and Yantosca, R. M.: Constraints from  $^{210}\text{Pb}$  and  $^7\text{Be}$  on wet deposition and transport in  
563 a global three-dimensional chemical tracer model driven by assimilated meteorological fields, *J. Geophys. Res.*  
564 *Atmos.*, 106, 12109-12128, <https://doi.org/10.1029/2000JD900839>, 2001.
- 565 Liu, H., Jacob Daniel, J., Bey, I., Yantosca Robert, M., Duncan Bryan, N., and Sachse Glen, W.: Transport pathways  
566 for Asian pollution outflow over the Pacific: Interannual and seasonal variations, *J. Geophys. Res. Atmos.*, 108,  
567 8786, <https://doi.org/10.1029/2002JD003102>, 2003.
- 568 Liu, Y., Park, R. J., Jacob, D. J., Li, Q., Kilaru, V., and Sarnat, J. A.: Mapping annual mean ground-level  $\text{PM}_{2.5}$   
569 concentrations using Multiangle Imaging Spectroradiometer aerosol optical thickness over the contiguous United  
570 States, *J. Geophys. Res. Atmos.*, 109, D22206, <https://doi.org/10.1029/2004JD005025>, 2004.
- 571 Luo, G., Yu, F., and Moch, J. M.: Further improvement of wet process treatments in GEOS-Chem v12.6.0: impact  
572 on global distributions of aerosols and aerosol precursors, *Geosci. Model Dev.*, 13, 2879-2903,  
573 <https://doi.org/10.5194/gmd-13-2879-2020>, 2020.
- 574 Luo, G., Yu, F., and Schwab, J.: Revised treatment of wet scavenging processes dramatically improves GEOS-Chem  
575 12.0.0 simulations of nitric acid, nitrate, and ammonium over the United States, *Geosci. Model Dev.*, 12, 3439-3447  
576 <https://doi.org/10.5194/gmd-12-3439-2019>, 2019.
- 577 Martin, R. V., Jacob, D. J., Yantosca, R. M., Chin, M., and Ginoux, P.: Global and regional decreases in  
578 tropospheric oxidants from photochemical effects of aerosols, *J. Geophys. Res. Atmos.*, 108, 4097,  
579 <https://doi.org/10.1029/2002JD002622>, 2003.
- 580 McNaughton, C. S., Clarke, A. D., Howell, S. G., Pinkerton, M., Anderson, B., Thornhill, L., Hudgins, C.,  
581 Winstead, E., Dibb, J. E., Scheuer, E., and Maring, H.: Results from the DC-8 Inlet Characterization Experiment  
582 (DICE): Airborne Versus Surface Sampling of Mineral Dust and Sea Salt Aerosols, *Aerosol Sci. Tech.*, 41, 136-159,  
583 <https://doi.org/10.1080/02786820601118406>, 2007.
- 584 McNaughton, C. S., Clarke, A. D., Kapustin, V., Shinozuka, Y., Howell, S. G., Anderson, B. E., Winstead, E., Dibb,  
585 J., Scheuer, E., Cohen, R. C., Wooldridge, P., Perring, A., Huey, L. G., Kim, S., Jimenez, J. L., Dunlea, E. J.,  
586 DeCarlo, P. F., Wennberg, P. O., Crounse, J. D., Weinheimer, A. J., and Flocke, F.: Observations of heterogeneous  
587 reactions between Asian pollution and mineral dust over the Eastern North Pacific during INTEX-B, *Atmos. Chem.*  
588 *Phys.*, 9, 8283-8308, <https://doi.org/10.5194/acp-9-8283-2009>, 2009.
- 589 Meng, J., Martin, R. V., Ginoux, P., Hammer, M., Sulprizio, M. P., Ridley, D. A., and van Donkelaar, A.: Grid-  
590 independent High Resolution Dust Emissions (v1.0) for Chemical Transport Models: Application to GEOS-Chem  
591 (version 12.5.0), *Geosci. Model Dev. Discuss.*, 1-23, <https://doi.org/10.5194/gmd-2020-380>, 2020.
- 592 Miao, R., Chen, Q., Zheng, Y., Cheng, X., Sun, Y., Palmer, P. I., Shrivastava, M., Guo, J., Zhang, Q., Liu, Y., Tan,  
593 Z., Ma, X., Chen, S., Zeng, L., Lu, K., and Zhang, Y.: Model bias in simulating major chemical components of  
594  $\text{PM}_{2.5}$  in China, *Atmos. Chem. Phys.*, 20, 12265-12284, <https://doi.org/10.5194/acp-20-12265-2020>, 2020.
- 595 Murray, L. T., Jacob, D. J., Logan, J. A., Hudman, R. C., and Koshak, W. J.: Optimized regional and interannual  
596 variability of lightning in a global chemical transport model constrained by LIS/OTD satellite data, *J. Geophys. Res.*  
597 *Atmos.*, 117, D20307, <https://doi.org/10.1029/2012JD017934>, 2012.
- 598 Nault, B. A., Campuzano-Jost, P., Day, D. A., Schroder, J. C., Anderson, B., Beyersdorf, A. J., Blake, D. R., Brune,  
599 W. H., Choi, Y., Corr, C. A., de Gouw, J. A., Dibb, J., DiGangi, J. P., Diskin, G. S., Fried, A., Huey, L. G., Kim, M.  
600 J., Knote, C. J., Lamb, K. D., Lee, T., Park, T., Pusede, S. E., Scheuer, E., Thornhill, K. L., Woo, J. H., and Jimenez,  
601 J. L.: Secondary organic aerosol production from local emissions dominates the organic aerosol budget over Seoul,  
602 South Korea, during KORUS-AQ, *Atmos. Chem. Phys.*, 18, 17769-17800, <https://doi.org/10.5194/acp-18-17769-2018>, 2018.
- 604 Pai, S. J., Heald, C. L., Pierce, J. R., Farina, S. C., Marais, E. A., Jimenez, J. L., Campuzano-Jost, P., Nault, B. A.,  
605 Middlebrook, A. M., Coe, H., Shilling, J. E., Bahreini, R., Dingle, J. H., and Vu, K.: An evaluation of global organic  
606 aerosol schemes using airborne observations, *Atmos. Chem. Phys.*, 20, 2637-2665, <https://doi.org/10.5194/acp-20-2637-2020>, 2020.



- 608 Park, R. J., Oak, Y. J., Emmons, L. K., Kim, C.-H., Pfister, G. G., Carmichael, G. R., Saide, P. E., Cho, S.-Y., Kim,  
609 S., Woo, J.-H., Crawford, J. H., Gaubert, B., Lee, H.-J., Park, S.-Y., Jo, Y.-J., Gao, M., Tang, B., Stanier, C. O.,  
610 Shin, S. S., Park, H. Y., Bae, C., and Kim, E.: Multi-model intercomparisons of air quality simulations for the  
611 KORUS-AQ campaign, *Elementa-Sci. Anthropol.*, 9, 00139, <https://doi.org/10.1525/elementa.2021.00139>, 2021.
- 612 Park Rokjin, J., Jacob Daniel, J., Field Brendan, D., Yantosca Robert, M., and Chin, M.: Natural and transboundary  
613 pollution influences on sulfate-nitrate-ammonium aerosols in the United States: Implications for policy, *J. Geophys.*  
614 *Res. Atmos.*, 109, D15204, <https://doi.org/10.1029/2003JD004473>, 2004.
- 615 Peterson, D. A., Hyer, E. J., Han, S.-O., Crawford, J. H., Park, R. J., Holz, R., Kuehn, R. E., Eloranta, E., Knote, C.,  
616 Jordan, C. E., and Lefer, B. L.: Meteorology influencing springtime air quality, pollution transport, and visibility in  
617 Korea, *Elementa-Sci. Anthropol.*, 7, 57, <https://doi.org/10.1525/elementa.395>, 2019.
- 618 Philip, S., Martin, R. V., Snider, G., Weagle, C. L., van Donkelaar, A., Brauer, M., Henze, D. K., Klimont, Z.,  
619 Venkataraman, C., and Guttikunda, S. K.: Anthropogenic fugitive, combustion and industrial dust is a significant,  
620 underrepresented fine particulate matter source in global atmospheric models, *Environ. Res. Lett.*, 12, 044018,  
621 <https://doi.org/10.1088/1748-9326/aa65a4>, 2017.
- 622 Podolske, J. R., Sachse, G. W., and Diskin, G. S.: Calibration and data retrieval algorithms for the NASA  
623 Langley/Ames Diode Laser Hygrometer for the NASA Transport and Chemical Evolution Over the Pacific  
624 (TRACE-P) mission, *J. Geophys. Res. Atmos.*, 108, 8792, <https://doi.org/10.1029/2002JD003156>, 2003.
- 625 Pye, H. O. T., Liao, H., Wu, S., Mickley, L. J., Jacob, D. J., Henze, D. K., and Seinfeld, J. H.: Effect of changes in  
626 climate and emissions on future sulfate-nitrate-ammonium aerosol levels in the United States, *J. Geophys. Res.*  
627 *Atmos.*, 114, D01205, <https://doi.org/10.1029/2008JD010701>, 2009.
- 628 Saide, P. E., Kim, J., Song, C. H., Choi, M., Cheng, Y., and Carmichael, G. R.: Assimilation of next generation  
629 geostationary aerosol optical depth retrievals to improve air quality simulations, *Geophys. Res. Lett.*, 41, 9188-9196,  
630 <https://doi.org/10.1002/2014GL062089>, 2014.
- 631 Saide, P. E., Gao, M., Lu, Z., Goldberg, D. L., Streets, D. G., Woo, J. H., Beyersdorf, A., Corr, C. A., Thornhill, K.  
632 L., Anderson, B., Hair, J. W., Nehrir, A. R., Diskin, G. S., Jimenez, J. L., Nault, B. A., Campuzano-Jost, P., Dibb, J.,  
633 Heim, E., Lamb, K. D., Schwarz, J. P., Perring, A. E., Kim, J., Choi, M., Holben, B., Pfister, G., Hodzic, A.,  
634 Carmichael, G. R., Emmons, L., and Crawford, J. H.: Understanding and improving model representation of aerosol  
635 optical properties for a Chinese haze event measured during KORUS-AQ, *Atmos. Chem. Phys.*, 20, 6455-6478,  
636 <https://doi.org/10.5194/acp-20-6455-2020>, 2020.
- 637 Scarino, A. J., Omland, M. D., Fast, J. D., Burton, S. P., Ferrare, R. A., Hostetler, C. A., Berg, L. K., Lefer, B.,  
638 Haman, C., Hair, J. W., Rogers, R. R., Butler, C., Cook, A. L., and Harper, D. B.: Comparison of mixed layer  
639 heights from airborne high spectral resolution lidar, ground-based measurements, and the WRF-Chem model during  
640 CalNex and CARES, *Atmos. Chem. Phys.*, 14, 5547-5560, <https://doi.org/10.5194/acp-14-5547-2014>, 2014.
- 641 Sekiyama, T. T., Tanaka, T. Y., Shimizu, A., and Miyoshi, T.: Data assimilation of CALIPSO aerosol observations,  
642 *Atmos. Chem. Phys.*, 10, 39-49, <https://doi.org/10.5194/acp-10-39-2010>, 2010.
- 643 Seinfeld, J. H. and Pandis, S. N.: *Atmospheric Chemistry and Physics: From Air Pollution to Climate Change*, Third  
644 Edition, Ch. 8, John Wiley & Sons, New Jersey, 2016.
- 645 Shah, V., Jacob, D. J., Moch, J. M., Wang, X., and Zhai, S.: Global modeling of cloud water acidity, precipitation  
646 acidity, and acid inputs to ecosystems, *Atmos. Chem. Phys.*, 20, 12223-12245, <https://doi.org/10.5194/acp-20-12223-2020>, 2020.
- 648 Travis, K. R., Crawford, J. H., Nault, B. A., Kim, H., Jordan, C. E., Chen, G., Zhai, S., Wang, X., Jimenez, J. L.,  
649 Dibb, J. E., Brune, W. H., Weinheimer, A., Wennberg, P., Long, R., Szykman, J. J., Woo, J. H., Kim, Y., Li, K.,  
650 McDuffie, E., Luo, G., Zhang, Q., Kim, S.: Why do models have difficulty simulating ammonium nitrate and nitric  
651 acid in East Asia?, manuscript in preparation.
- 652 van Donkelaar, A., Martin Randall, V., Brauer, M., and Boys Brian, L.: Use of Satellite Observations for Long-  
653 Term Exposure Assessment of Global Concentrations of Fine Particulate Matter, *Environ. Health Perspect.*, 123,  
654 135-143, <https://doi.org/10.1289/ehp.1408646>, 2015.
- 655 van Donkelaar, A., Martin, R. V., Brauer, M., Hsu, N. C., Kahn, R. A., Levy, R. C., Lyapustin, A., Sayer, A. M., and  
656 Winker, D. M.: Global Estimates of Fine Particulate Matter using a Combined Geophysical-Statistical Method with



- 657 Information from Satellites, Models, and Monitors, *Environ. Sci. Technol.*, 50, 3762-3772,  
658 <https://doi.org/10.1021/acs.est.5b05833>, 2016.
- 659 van der Werf, G. R., Randerson, J. T., Giglio, L., van Leeuwen, T. T., Chen, Y., Rogers, B. M., Mu, M., van Marle,  
660 M. J. E., Morton, D. C., Collatz, G. J., Yokelson, R. J., and Kasibhatla, P. S.: Global fire emissions estimates during  
661 1997–2016, *Earth Syst. Sci. Data*, 9, 697-720, <https://doi.org/10.5194/essd-9-697-2017>, 2017.
- 662 Wang, Q., Jacob, D. J., Fisher, J. A., Mao, J., Leibensperger, E. M., Carouge, C. C., Le Sager, P., Kondo, Y.,  
663 Jimenez, J. L., Cubison, M. J., and Doherty, S. J.: Sources of carbonaceous aerosols and deposited black carbon in  
664 the Arctic in winter-spring: implications for radiative forcing, *Atmos. Chem. Phys.*, 11, 12453-12473,  
665 <https://doi.org/10.5194/acp-11-12453-2011>, 2011.
- 666 Wang, Q., Jacob, D. J., Spackman, J. R., Perring, A. E., Schwarz, J. P., Moteki, N., Marais, E. A., Ge, C., Wang, J.,  
667 and Barrett, S. R. H.: Global budget and radiative forcing of black carbon aerosol: Constraints from pole-to-pole  
668 (HIPPO) observations across the Pacific, *J. Geophys. Res. Atmos.*, 119, 195-206,  
669 <https://doi.org/10.1002/2013JD020824>, 2014.
- 670 Wang, X., Heald, C. L., Ridley, D. A., Schwarz, J. P., Spackman, J. R., Perring, A. E., Coe, H., Liu, D., and Clarke,  
671 A. D.: Exploiting simultaneous observational constraints on mass and absorption to estimate the global direct  
672 radiative forcing of black carbon and brown carbon, *Atmos. Chem. Phys.*, 14, 10989-11010,  
673 <https://doi.org/10.5194/acp-14-10989-2014>, 2014.
- 674 Wang, Y., Zhang, Q., Jiang, J., Zhou, W., Wang, B., He, K., Duan, F., Zhang, Q., Philip, S., and Xie, Y.: Enhanced  
675 sulfate formation during China's severe winter haze episode in January 2013 missing from current models, *J.*  
676 *Geophys. Res. Atmos.*, 119, 425-410,440, <https://doi.org/10.1002/2013JD021426>, 2014.
- 677 Wei, J., Li, Z., Lyapustin, A., Sun, L., Peng, Y., Xue, W., Su, T., and Cribb, M.: Reconstructing 1-km-resolution  
678 high-quality PM<sub>2.5</sub> data records from 2000 to 2018 in China: spatiotemporal variations and policy implications,  
679 *Remote Sens. Environ.*, 252, 112136, <https://doi.org/10.1016/j.rse.2020.112136>, 2021.
- 680 Woo, J.-H., Kim, Y., Kim, H.-K., Choi, K.-C., Eum, J.-H., Lee, J.-B., Lim, J.-H., Kim, J., and Seong, M.:  
681 Development of the CREATE Inventory in Support of Integrated Climate and Air Quality Modeling for Asia,  
682 *Sustainability*, 12, 7930, <https://doi.org/10.3390/su12197930>, 2020.
- 683 Zhai, S., Jacob, D. J., Wang, X., Shen, L., Li, K., Zhang, Y., Gui, K., Zhao, T., and Liao, H.: Fine particulate matter  
684 (PM<sub>2.5</sub>) trends in China, 2013-2018: separating contributions from anthropogenic emissions and meteorology,  
685 *Atmos. Chem. Phys.*, 19, 11031-11041 <https://doi.org/10.5194/acp-19-11031-2019>, 2019.
- 686 Zhai, S., Jacob, D. J., Wang, X., Liu, Z., Wen, T., Shah, V., Li, K., Moch, J. M., Bates, K. H., Song, S., Shen, L.,  
687 Zhang, Y., Luo, G., Yu, F., Sun, Y., Wang, L., Qi, M., Tao, J., Gui, K., Xu, H., Zhang, Q., Zhao, T., Wang, Y., Lee,  
688 H. C., Choi, H., and Liao, H.: Control of particulate nitrate air pollution in China, *Nat. Geosci.*,  
689 <https://doi.org/10.1038/s41561-021-00726-z>, 2021.
- 690 Zhang, L., Kok, J. F., Henze, D. K., Li, Q., and Zhao, C.: Improving simulations of fine dust surface concentrations  
691 over the western United States by optimizing the particle size distribution, *Geophys. Res. Lett.*, 40, 3270-3275,  
692 <https://doi.org/10.1002/grl.50591>, 2013.
- 693 Zhang, L., Gong, S., Padro, J., and Barrie, L.: A size-segregated particle dry deposition scheme for an atmospheric  
694 aerosol module, *Atmos. Environ.*, 35, 549-560, [https://doi.org/10.1016/S1352-2310\(00\)00326-5](https://doi.org/10.1016/S1352-2310(00)00326-5), 2001.
- 695 Zhang, X., Wang, H., Che, H.-Z., Tan, S.-C., Shi, G.-Y., and Yao, X.-P.: The impact of aerosol on MODIS cloud  
696 detection and property retrieval in seriously polluted East China, *Sci. Total Environ.*, 711, 134634,  
697 <https://doi.org/10.1016/j.scitotenv.2019.134634>, 2020.
- 698 Zheng, B., Tong, D., Li, M., Liu, F., Hong, C., Geng, G., Li, H., Li, X., Peng, L., Qi, J., Yan, L., Zhang, Y., Zhao,  
699 H., Zheng, Y., He, K., and Zhang, Q.: Trends in China's anthropogenic emissions since 2010 as the consequence of  
700 clean air actions, *Atmos. Chem. Phys.*, 18, 14095-14111, <https://doi.org/10.5194/acp-18-14095-2018>, 2018.
- 701 Ziemba, L. D., Lee Thornhill, K., Ferrare, R., Barrick, J., Beyersdorf, A. J., Chen, G., Crumeyrolle, S. N., Hair, J.,  
702 Hostetler, C., Hudgins, C., Obland, M., Rogers, R., Scarino, A. J., Winstead, E. L., and Anderson, B. E.: Airborne  
703 observations of aerosol extinction by in situ and remote-sensing techniques: Evaluation of particle hygroscopicity,  
704 *Geophys. Res. Lett.*, 40, 417-422, <https://doi.org/10.1029/2012GL054428>, 2013.